JGR Space Physics

RESEARCH ARTICLE
10.1029/2021JA029909

Key Points:

- NASA-Global-scale observations of the limb and disk obtained far-ultra-violet nightglow images of rocket exhaust depletion (RED)
- Magnetic field strength increased inside the RED
- Ionospheric slab thickness increased inside the RED

Correspondence to:

J. Park,
pj@kasi.re.kr

Citation:

Park, J., Rajesh, P. K., Ivarsen, M. F., Lin, C. C. H., Eastes, R. W., Chao, C. K., et al. (2022). Coordinated observations of rocket exhaust depletion: GOLD, Madrigal TEC, and multiple low-Earth-orbit satellites. *Journal of Geophysical Research: Space Physics*, *127*, e2021JA029909. https://doi.org/10.1029/2021JA029909

Received 25 AUG 2021
Accepted 6 JAN 2022

The copyright line for this article was changed on 8 OCT 2022 after original online publication.

Author Contributions:

Conceptualization: Jaeheung Park
Data curation: P. K. Rajesh, Magnus F. Ivarsen, Charles C. H. Lin, Richard W. Eastes, Chi Kuang Chao, Anthea J. Coster, Lasse Clausen, Johnathan K. Burchill
Formal analysis: Jaeheung Park, Magnus F. Ivarsen
Funding acquisition: Charles C. H. Lin, Richard W. Eastes, Chi Kuang Chao, Anthea J. Coster, Lasse Clausen
Investigation: Jaeheung Park, Magnus F. Ivarsen
Project Administration: Charles C. H. Lin, Richard W. Eastes, Anthea J. Coster, Lasse Clausen

Coordinated Observations of Rocket Exhaust Depletion: GOLD, Madrigal TEC, and Multiple Low-Earth-Orbit Satellites

Jaeheung Park[1,2], P. K. Rajesh[3], Magnus F. Ivarsen[4], Charles C. H. Lin[3], Richard W. Eastes[5], Chi Kuang Chao[6], Anthea J. Coster[7], Lasse Clausen[4], and Johnathan K. Burchill[8]

[1]Space Science Division, Korea Astronomy and Space Science Institute, Daejeon, South Korea, [2]Department of Astronomy and Space Science, Korea University of Science and Technology, Daejeon, South Korea, [3]Department of Earth Sciences, National Cheng Kung University, Tainan, Taiwan, [4]Department of Physics, University of Oslo, Oslo, Norway, [5]Laboratory for Atmospheric and Space Physics, University of Colorado Boulder, Boulder, CO, USA, [6]Department of Space Science and Engineering, National Central University, Chung-Li, Taiwan, [7]Haystack Observatory, Massachusetts Institute of Technology, Cambridge, MA, USA, [8]Department of Physics and Astronomy, University of Calgary, Calgary, AB, Canada

Abstract A plasma density hole was created in the ionosphere by a rocket launch from Cape Canaveral, Florida near local sunset on 30 August 2020, which is called rocket exhaust depletion (RED). The hole persisted for several hours into the night and was observed in total electron content (TEC) maps, the Global-scale Observations of the Limb and Disk (GOLD) imager, and multiple low-earth-orbit satellites. The RED created a nightglow pit in the GOLD 135.6 nm image. Swarm satellites found that the RED exhibited insignificant changes in electron/ion temperature and field-aligned currents. On the other hand, magnetic field strength was enhanced inside the RED by a few tenths of a nanotesla. Assimilation data products of the Constellation Observing System for Meteorology, Ionosphere, and Climate 2 (COSMIC-2) mission reveal that ionospheric slab thickness increased at the center of the RED, which is supported by combined analyses of the GOLD and TEC data. The RED did not host conspicuous substructures that are stronger and longer-lasting than the ambient plasma did.

Plain Language Summary Water molecules abundant in rocket exhaust are known to expedite loss of charged particles, which leads to a big hole in the ionosphere, so-called rocket exhaust depletion (RED). On 30 August 2020, a massive rocket was launched from Cape Canaveral, Florida around local sunset time. As expected, the launch created RED in plasma data obtained by ground-based global positioning system receivers and by multiple low-Earth-orbit satellites at altitudes of several hundreds of kilometers above ground. As the RED persisted into the night, the global-scale observations of the limb and disk imager flying ~36,000 km above the American continent acquired a 2-dimensional image at the 135.6 nm light wavelength (i.e., color). The Swarm satellites found that magnetic field strength increased by a few tenths of a nanotesla at the RED. Combined analyses of the observation data reveal that the vertical thickness of the ionosphere increased in the middle of the RED. The RED did not host conspicuous substructures that are stronger and longer-lasting than the ambient plasma did.

1. Introduction

Rocket launches are known to leave a number of signatures in the ionosphere and upper atmosphere. The fast moving rocket bodies first generate shock and acoustic waves (e.g., Chou et al., 2018; Kakinami et al., 2013; Lin et al., 2017; Liu et al., 2018). Also, water molecules released as rocket exhaust can enhance chemical recombination of ionospheric plasma (e.g., Bernhardt et al., 2001), which is called Rocket Exhaust Depletions (REDs): see Mendillo et al. (2008). As a byproduct of the recombination process, excited oxygen atoms are created, which eventually emit 630.0 nm red airglow (e.g., Mendillo et al., 2008). Under daylight, the water molecules in the exhaust are also photo-dissociated to produce hydrogen atoms, which in turn scatter the Lyman-alpha line (121.6 nm) in the sunlight (e.g., Meier et al., 2011).

RED, which will be the focus of this paper, has been studied for more than 60 years with various instruments: ionosondes (e.g., Booker, 1961; Mendillo et al., 2008), Incoherent Scatter Radar (ISR: e.g., Wand & Mendillo, 1984),

Software: Jaeheung Park, P. K. Rajesh, Magnus F. Ivarsen, Chi Kuang Chao
Validation: P. K. Rajesh, Charles C. H. Lin
Visualization: P. K. Rajesh, Magnus F. Ivarsen
Writing – original draft: Jaeheung Park
Writing – review & editing: Jaeheung Park, P. K. Rajesh, Magnus F. Ivarsen, Charles C. H. Lin, Richard W. Eastes, Chi Kuang Chao, Anthea J. Coster, Lasse Clausen, Johnathan K. Burchill

Global Position System (GPS) receivers (e.g., Choi & Kil, 2017; Mendillo et al., 2008; Ssessanga et al., 2018), airglow imagers (e.g., Mendillo et al., 2008), and in-situ measurements by low-Earth-orbit (LEO) satellites (e.g., Mendillo et al., 2008; Park et al., 2016). Computer simulations have also been conducted extensively, such as Bernhardt et al. (2001), Lin et al. (2017), and Feng et al. (2021), to name a few. Furthermore, the effects of RED on radio wave propagation were studied by, for example, Ma et al. (2021). It is known that RED can last for several hours, even under daylight and concomitant refilling by photo-ionization (e.g., Park et al., 2016, and references therein).

Two-dimensional (2D) RED imaging on the world map heavily counted on the total electron content (TEC) data obtained from global navigation satellite system (GNSS) receivers (e.g., Liu et al., 2018; Mendillo et al., 2008; Nakashima & Heki, 2014; Park et al., 2016). In addition, there were studies based on airglow images. Mendillo et al. (2008) reported that nighttime 630.0 nm airglow was enhanced along a RED trajectory, which was interpreted as representing oxygen atoms excited by chemical recombination processes of RED. For several space transport system (STS) launches, Stevens et al. (2005) and Meier et al. (2010, 2011) reported 2D dayglow images of rocket exhaust in the Lyman-alpha line (121.6 nm). The emission comes from sunlight scattered by hydrogens (e.g., Vorburger & Wurz, 2021, Table 3), which result from dissociation of H_2O in rocket exhaust (Stevens et al., 2005) and can be used as tracers of atmospheric transport (e.g., Datta-Barua et al., 2021). Niciejewski et al. (2011) also presented 2D images of the RED in the H_2O microwave brightness. Note that those H− or H_2O− related emissions represent rocket exhaust itself (i.e., neutral particles) rather than the ionospheric depletion it induces (i.e., charged particles). To the best of the authors' knowledge, it is yet to be reported how RED would look in 2D nightglow images in the far-ultra-violet (FUV) wavelength regime, for example, in the 135.6 nm oxygen line and the N_2 Lyman-Birge-Hopfield (LBH) band.

In-situ observations of RED have also been rare (see discussion of Park et al., 2016), but such measurements can be more beneficial for investigating detailed spatial structures of RED than remote sensing, which inherently integrates signals along the line-of-sight (LOS). Park et al. (2016) reported in-situ measurements of "dayside" RED, which is naturally expected to have smooth density profiles because photo-ionization creates a harsh environment for ionospheric irregularities to survive (e.g., Huang et al., 2013, discussion). For nightside RED, Mendillo et al. (1980) briefly mentioned absence of RED substructures at >1 km scale sizes. Still, it is yet to be investigated using in-situ data whether “nightside” RED can host significant substructures, or they are smooth like dayside RED events.

Only a few papers addressed RED plasma parameters other than density, such as ion and electron temperature. Bernhardt and Sulzer(2004, Figures 6–7) reported enhanced ion temperature and field-aligned ion upflow around a nightside RED. But, the duration of the enhancement was much shorter than that of RED, which suggests that the ion velocity and temperature perturbations be associated to the initial development of RED. Bernhardt et al. (2012, Figure 27) presented in-situ observations of various plasma parameters (e.g., velocity and temperature) around a rocket exhaust region, but the plasma density there was enhanced rather than depleted, which implies that the event represents other exhaust-related phenomena than RED itself. Park et al. (2015, 2016) showed that electron temperature observed by LEO satellites was enhanced at a “dayside” RED. Such anti-correlation between “dayside” electron temperature and density has been reported for other natural ionospheric phenomena, such as Oyama et al. (1988, Figure 6) for Equatorial Plasma Bubbles (EPBs). As the electron density-temperature relationship changes with local time (Oyama et al., 1988, Figure 6; Kakinami et al., 2011, Figure 1), further studies are necessary for investigating electron temperature variations around nightside RED.

As for magnetic signatures of REDs, only Park et al. (2015) briefly addressed absence of noticeable diamagnetic effect (i.e., compressional component of magnetic perturbation) of a “dayside” RED. There has been no report on field-aligned current (FAC) signatures around REDs, which lead to magnetic deflections perpendicular to the background field lines. In the low- and mid-latitude ionosphere, localized FACs generally signify divergence of ambient ionospheric currents by plasma conductivity inhomogeneity (e.g., Rodríguez-Zuluaga & Stolle, 2019; Stolle et al., 2006).

In this study, the above-mentioned knowledge gaps will be addressed in detail. The Global-scale Observations of the Limb and Disk (GOLD) mission is used for getting 2D FUV images of nightglow intensity in the 135.6 nm line and the LBH band. From regional 2D maps of TEC combined with the GOLD data, we try to extract constraints on the vertical profiles of ionospheric plasma. The results will be cross-compared with assimilative

3-dimensional (3D) ionospheric density products from the Constellation Observing System for Meteorology, Ionosphere, and Climate 2 (COSMIC-2) mission. In-situ measurements by multiple LEO satellites provide plasma density data at multiple locations as well as other plasma parameters: for example, electron/ion temperature and magnetic field changes.

2. Datasets and Processing Methods

The GOLD mission aims at imaging the upper atmosphere/ionosphere above American/Atlantic regions in the FUV range. The instrument is carried by a geosynchronous (GEO) satellite (SES-14) at 47.5°W in geographic longitude since 2018. The operation sequence is nominally composed of four individual modes: dayside disk, nightside disk, limb, and occultation modes (Eastes et al., 2020). In this study, nightside disk images of an RED event are investigated, especially in the 135.6 nm line representing the ionospheric plasma density (Qin et al., 2015). The data repository of the GOLD mission is at: https://gold.cs.ucf.edu/data/search/.

The Massachusetts institute of technology (MIT) Haystack observatory produces 2D maps of TEC with a spatial resolution of $1° \times 1°$ in geographic latitudes (GLAT) and longitudes (GLON) every 5 min: see Coster et al. (2017) and references therein. The product is based on ground-based GNSS receivers, and the coverage is better over landmasses than over the ocean. All the data are open to the public at Madrigal web sites, such as: http://cedar.openmadrigal.org/openmadrigal.

The Swarm constellation, which was launched on 22 November 2013, has 3 satellites equipped with precision magnetometers and plasma probes. Two of the satellites (Swarm-Alpha and Swarm-Charlie) fly side-by-side at an altitude of about 450 km while the remaining one (Swarm-Bravo) is about 50 km above the pair. In this study, the electron density and temperature (2 Hz; product identifier "EFIx_LP_1B", where x is A, B, or C to signify one of the three Swarm satellites) measured by the onboard Langmuir Probes (LPs) are mainly used to diagnose the plasma around the RED event: refer to Knudsen et al. (2017) for details of the instrument. We also seek for the existence of measurable magnetic field deflections, which represent local current systems caused by the RED event. The Swarm data are available at: https://swarm-diss.eo.esa.int/#swarm.

The COSMIC-2 mission is composed of 6 identical satellites having a target altitude of about 520 km and inclination angle of 24°. The satellites were launched in June 2019 into a parking orbit at an altitude of about 720 km, and have been pulled down to the mission height gradually. Each satellite carries the Ion Velocity Meter (IVM) that can measure ion density, temperature, and velocity vectors. Currently, only the ion density are available at the official repository (https://data.cosmic.ucar.edu/gnss-ro/cosmic2/postProc/level2/), which will be used for this study. The COSMIC-2 project also provides the global ionospheric specification (GIS) product, a 3-dimensional cube of electron density per hour, which is created by assimilating COSMIC-2 radio occultation (RO) observations with ground-based TEC (e.g., Rajesh et al., 2021). All the GIS data are open to the registered users at http://formosat7.earth.ncku.edu.tw/.

Norsat-1, which was launched on 14 July 2017 into a Sun-synchronous circular (altitude∼600 km; local time∼23:30) orbit, carries multi-Needle Langmuir Probe (mNLP) for electron density and temperature measurements (Hoang et al., 2018). The data and orbit files are available at the data distribution site (http://tid.uio.no/plasma/norsat/data.php). As was done by Ivarsen, Park, et al. (2021), we utilize the raw probe current that represents plasma density because only relative variations are important in this study.

3. Results

3.1. Overview of the RED Event: Time Series of 2D TEC Images

On 30 August 2020, a Falcon rocket was launched from Cape Canaveral, Florida at 23:18:56 in Universal Time (UT): https://en.wikipedia.org/wiki/2020_in_spaceflight. It is notable that the rocket was shot into a polar orbit, for the first time since the last similar launch from Cape Canaveral in 1969. The geomagnetic activity was slightly enhanced during the period of interest: the Kp index was between 2.7 and 4.3. As is expected (e.g., Chou et al., 2018; Mendillo et al., 2008), the rocket left a signature of plasma depletion in the ionosphere, so-called RED.

Figure 1 presents the temporal evolution of TEC around Cape Canaveral. In each panel, the color palette represents TEC, and the large cross on Florida corresponds to the launch site. In order to display the RED under a unified color palette, we intentionally use a saturated color bar. The gray dashed grids signify magnetic latitudes (MLAT) and longitudes (MLON) in the Quasi-Dipole coordinate system (Laundal & Richmond, 2017) while the thick black dash-dotted ropes in the top row indicate the solar zenith angle (SZA) of 90°, that is, approximate location of the sunset terminator. On the maps, thick solid black lines with picket fences are LEO satellite orbits projected along magnetic field lines down to the nominal Madrigal TEC altitude of 350 km. We assume that the Earth's radius is 6371.2 km. The CHAOS geomagnetic field model (https://www.space.dtu.dk/english/research/scientific_data_and_models/magnetic_field_models) is used for the mapping. Black picket fences running along the mapped orbits indicate relative variations of the in-situ plasma density measured by individual satellites. Every panel that shows the LEO satellite track has a subpanel at the bottom or to the right. The subpanels give qualitative comparison between the in-situ plasma density (black) and the TEC values resampled along the mapped satellite track (red).

Figure 1a reveals a faint signature of TEC depletion to the south of the launch site, which is highlighted with a green arrow. Note that Figure 1 corresponds to the time no more than 10 min after the launch, and that the depletion emerged before local sunset. Further, 10 minutes later, in Figure 1b, the RED becomes more conspicuous. Again 30 min later (Figure 1c), the mapped orbit of COSMIC-2D passed through the RED from west to east. In the bottomside subpanel of Figure 1c, RED signatures in the in-situ plasma density (black) and TEC (red) are at similar locations. About 1.17 hr later (Figure 1d), the RED signature in the TEC map persisted, and Swarm-Alpha and Swarm-Charlie pair skimmed the eastward half of the RED. For visual clarity, we only show the Swarm-Alpha's orbit and data in Figure 1d. In the rightside subpanel of Figure 1d, the in-situ plasma density (black) and resampled TEC (red) show reasonably good agreement. Half an hour later (Figure 1e), COSMIC-2D again passed above the RED, and the COSMIC-2D and TEC data reasonably agree with each other. Further 1.17 hr later (Figure 1f), Norsat-1 passed around the RED and observed plasma density depletion (rightside subpanel). Note that the original data are resampled at 2 Hz rate to reduce the data size. The location of the minimum in-situ density (refer to the red arrow in Figure 1f) is close to the region where RED was observed by COSMIC-2D, and the TEC map in Figure 1e. Total Electron Content resampled along the Norsat-1 orbit is not shown because of large data gaps in the TEC map. In summary, (a) the TEC maps in Figure 1 exhibit RED for more than 3 hours, and (b) in-situ plasma density measurements around the RED are in good agreement with what the TEC maps show.

3.2. Nightglow Images From GOLD

At 00:25 UT on 31 August 2020, about 1 hr after the rocket launch, GOLD obtained 1 figure around the RED event. Before taking this picture, the field-of-view (FOV) of GOLD was directed toward Africa and Atlantic Ocean, and it could not fully observe the RED. After 00:25 UT, on the other hand, the normal operation scenario turned GOLD off in order to avoid direct sunlight touching its sensitive parts. Therefore, the image at 00:25 UT on 31 August 2020 (Figure 2) is the only one that captured the conspicuous RED signatures.

Figure 2a presents a 135.6 nm nightglow image obtained by GOLD, in which Level-1C data integrated over 133.0 nm ∼ 137.0 nm are interpolated at regular GLAT-GLON grids without additional corrections for emission angles. The thick white contour corresponds to the 3 Rayleigh level of the image after smoothing by a 17-by-17 median filter. The image reveals an oval-like depletion of the nightglow around the launch site, in agreement with the TEC maps in Figure 1 (especially, with Figure 1c that is close in time to Figure 2). The oval-like morphology of the 135.6 nm depletion is different from characteristics of natural irregularities in the mid-latitude ionosphere, which have been generally reported to be planar (e.g., Aa et al., 2019; Chartier et al., 2021; Cherniak & Zakharenkova, 2018; Kil et al., 2019; Zakharenkova et al., 2016). The LBH band image (Figure 2b) does not have a noticeable RED signature. LBH band nightglow around Cape Canaveral appears weak and noisy, as expected for the nightside low- and mid-latitude ionosphere hosts few energetic particles. Note that the saturated dark red region on the left edge of the GOLD images corresponds to sunlight contamination. The white dashed line in each panel is reserved for direct comparison between TEC and 135.6 nm nightglow, which will be addressed in Section 4.

As the day of interest (30–31 August 2020) was close to the full moon (on 25 August 2020; https://www.calendardate.com/moon_phases/2020/august.php), most of the ground-based all-sky imagers could not obtain clear nightglow images: for example, the all-sky imager at Arecibo (http://sirius.bu.edu/dataview/?location=arecibo&-

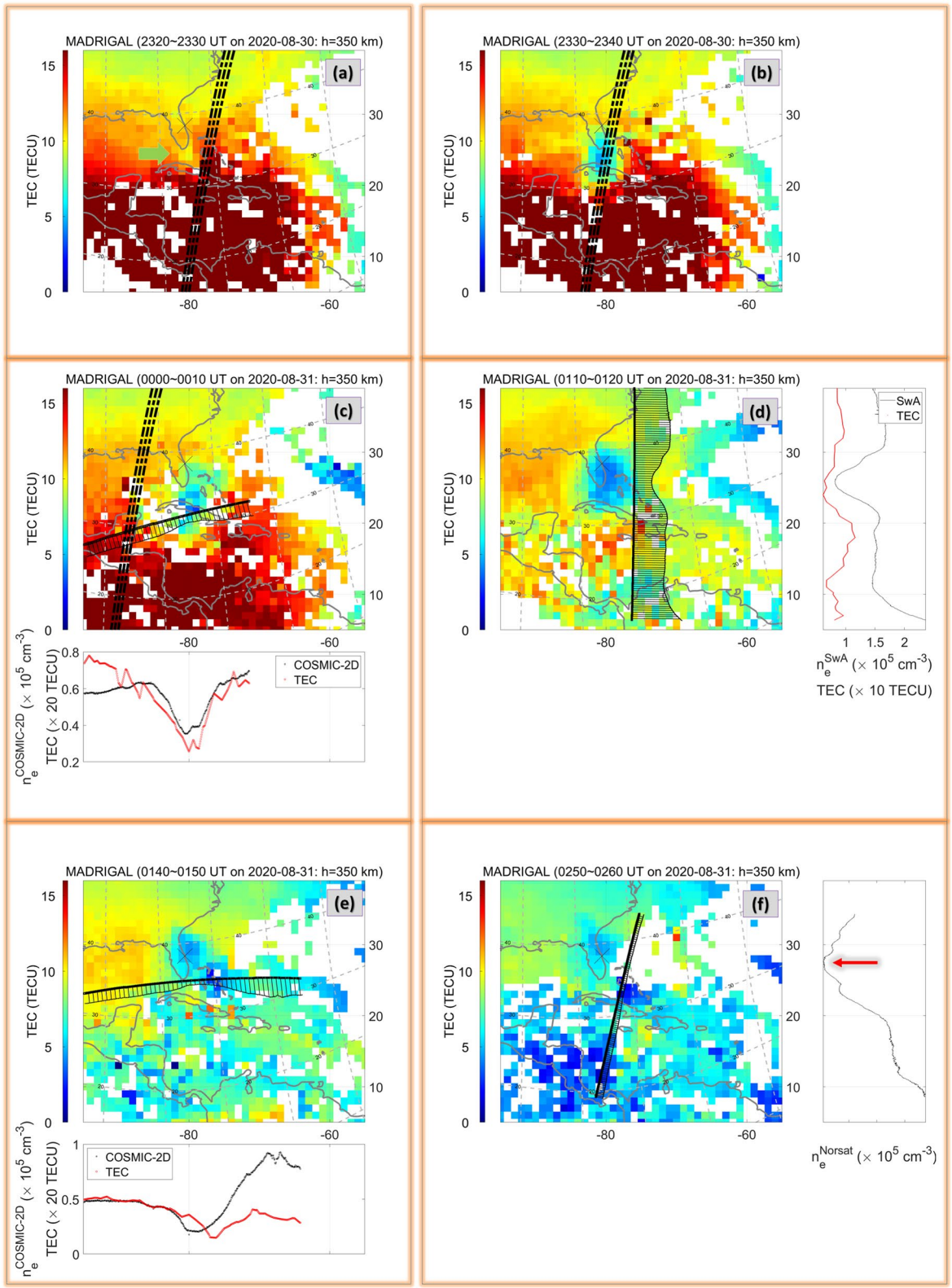

Figure 1.

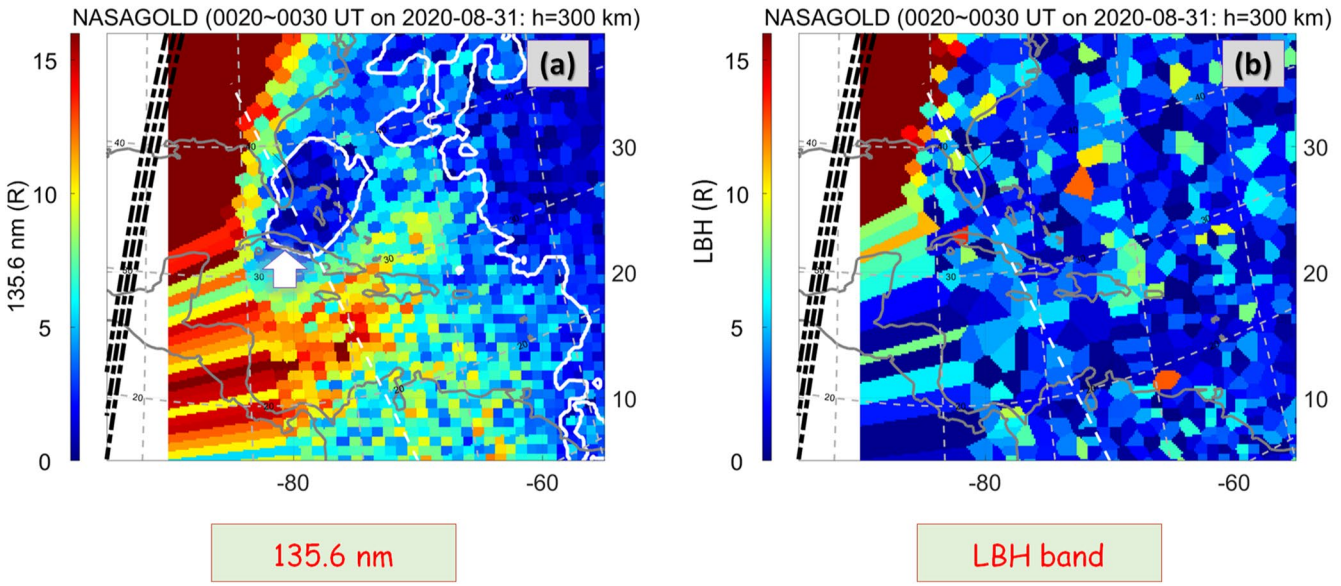

Figure 2. Global-scale observations of the limb and disk observations of far-ultra-violet nightglow around the launch site: (a) 135.6 nm Oxygen line, and (b) Lyman-Birge-Hopfield band. Thick white contours in panel (a) are given for visual guidance and corresponds to the 3 Rayleigh level of the image after smoothing by a 17-by-17 median filter. The white arrow points out the rocket exhaust depletion location. Saturated dark red color on the left part of panel a represents sunlight contamination close to the terminator.

year=2020&filt=6300). On the other hand, GOLD observing the ionosphere from the GEO vantage point could image the RED with negligible moonlight contamination, which evidences the usefulness of GOLD in complementing conventional ground-based imagers.

3.3. Plasma Temperature and FAC Variations: Swarm Observation 1

The good agreement between the TEC and in-situ plasma density (Figure 1) suggests that COSMIC-2D, Swarm, and Norsat-1 actually encountered the same RED as the TEC maps reveal. Hence, we move one step further to investigate RED properties other than plasma abundance. In this and the following subsections, we mainly focus on the electron temperature and geomagnetic field measured by Swarm-Alpha and Swarm-Charlie. The Swarm pair observations are shown in Figure 3: Swarm-Alpha in red, and Swarm-Charlie in blue. Each panel from the top presents: (a) Plasma density, (b) electron temperature, (c) floating potential of the LP, (d) radial current density, and (e) satellite track on the world map rotated clockwise by 90°. The thick black dashed line in the bottom panel represents the dip equator, and the horizontal axis is GLAT. The RED event is highlighted by the red shade.

In Figure 3a, we can see that the RED is deeper in the Swarm-Alpha data (red line) than for Swarm-Charlie (blue line), which can be understood in terms of the distance to the launch pad: Refer to Figure 3e. Swarm-Alpha was located closer to the launch pad than Swarm-Charlie. For comparison, note that the Swarm pair near the dip equator encountered EPBs that exhibit strong fluctuations of plasma density and clear inter-satellite difference (gray shade).

The electron temperature in Figure 3b does not show drastic changes around the RED, except for small notch-like artefacts that are spread over a large part of this orbit. The absence of an electron temperature increase is notable because the two dayside RED events in Park et al. (2015, 2016) exhibited clear enhancements of electron temperature. It may be interpreted in terms of solar Extreme Ultra-Violet (EUV) heating and collisional cooling

Figure 1. Temporal evolution of the rocket exhaust depletion event around Cape Canaveral on 30–31 August 2020. The panels are ordered in universal time. In each panel, the color palette represents vertical total electron content (TEC) obtained from the Madrigal database. The gray dashed grid corresponds to magnetic latitudes and longitudes while one cross is placed at the launch site. The thick black dot-dashed ropes represent the solar zenith angle of 89.5°, 90°, and 90.5°, which approximately corresponds to the dusk terminator. Solid black curves stand for the satellite tracks projected along geomagnetic field lines down to 350 km, the nominal mapping altitude of the Madrigal TEC. The accompanied picket fence structures in panels c–f qualitatively show in-situ plasma density. The bottomside and rightside subpanels give comparison between in-situ plasma density (black) and TEC resampled along the spacecraft tracks (red).

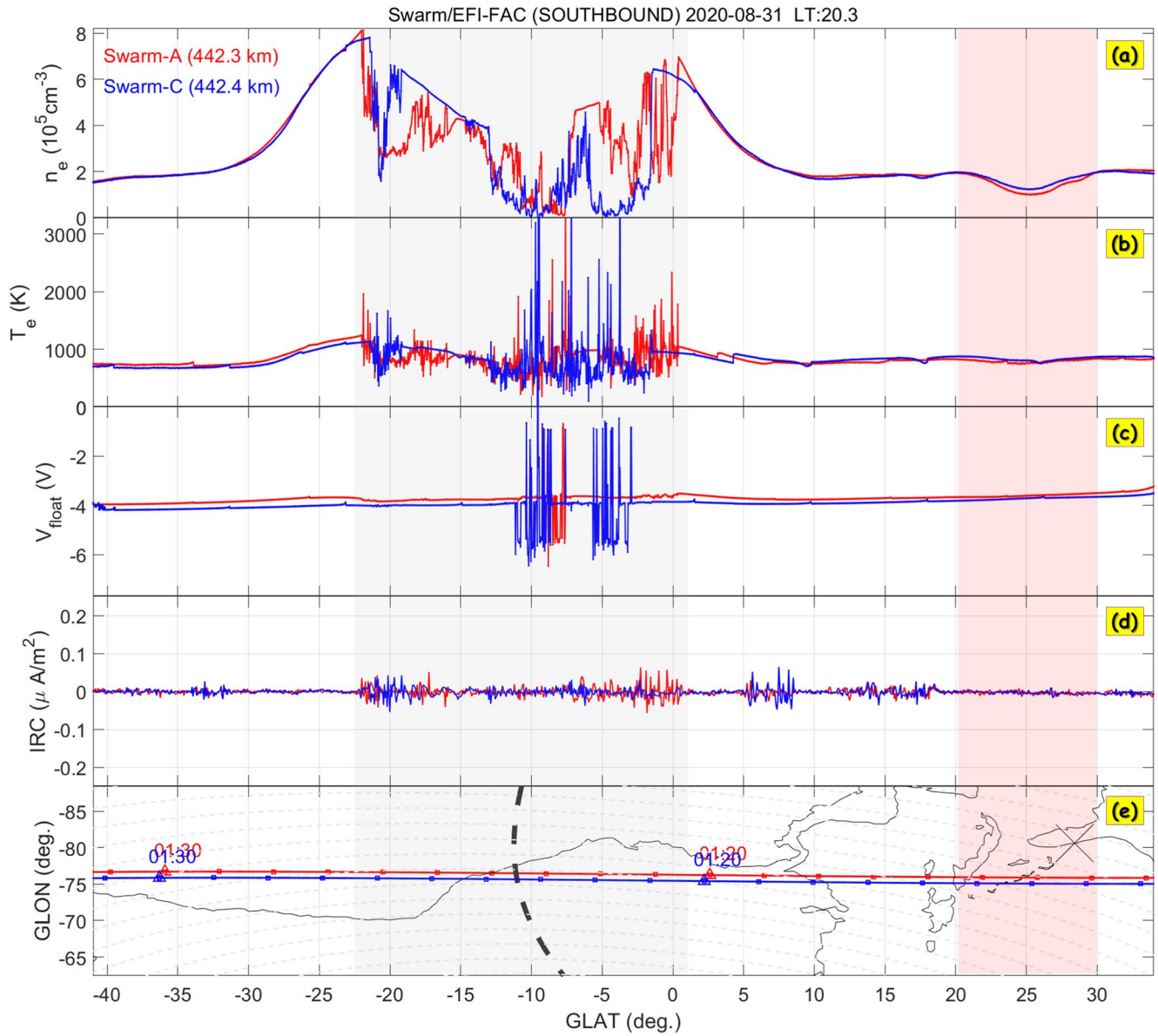

Figure 3. In-situ observations of the rocket exhaust depletion (RED) by Swarm-Alpha (red line) and Swarm-Charlie (blue line): (a) Plasma density, (b) electron temperature, (c) floating potential of the onboard Langmuir Probe, (d) radial current density, and (e) spacecraft ground tracks rotated clockwise by 90°. The universal time tags are given at regular 10 min intervals on the tracks. The gray and pink shades correspond to regions hosting equatorial plasma bubbles and RED, respectively.

in the ionosphere. During daytime, the electron temperature increases when the electron density decreases due to the balance between solar EUV heating and electron cooling by the Coulomb collision with ions. On the contrary, during nighttime when the solar heating disappears, this competition mechanism does not work. The floating potential of the LP, which is largely determined by the electron temperature (e.g., Chen, 2003, Equation 5; Bhattarai, 2017, Equation 8), also shows little RED-related change. According to Swarm ion temperature data that have lately been released (Lomidze et al., 2021), ion temperature also exhibits inconspicuous changes at the RED (figure not shown).

Plasma density and electron temperature measured by the Swarm/LP were extensively investigated by Lomidze et al. (2018). Their validation of electron temperature relied on Swarm conjunctions with low-latitude incoherent scatter radars. Swarm temperatures are systematically too high by several hundred Kelvin, and Lomidze et al. (2018) provide expressions for adjusting the electron temperatures to bring them into agreement with ISR observations on average: the expressions are used for Figures 3 and 4 in our study. The recent statistical investigation by

Pignalberi et al. (2021) examines the Swarm temperatures in terms of local time at three ISR sites. They report that the Lomidze et al. corrected temperatures are still systematically higher than ISR estimates for night-time and low-latitude observations. The location and local time of the RED analyzed in this study, however, are consistent with the region of good electron temperature data quality. Rodríguez-Zuluaga et al. (2019) noted the Swarm/LP electron temperature may exhibit strong and suspicious fluctuations around EPBs. This is also the case for the EPBs in our Figure 3 (gray shaded), and the fluctuation magnitudes reach a few thousand Kelvin. Caution is urged in interpreting those EPB-related data. However, in the RED in Figure 3 (red shaded), which is the region of our main interest, the electron temperatures vary smoothly and there are no intense fluctuations. Therefore, the authors believe that the Swarm/LP data around the RED are reliable, which will be further discussed in the next subsection.

Figure 3d presents the radial current density calculated from the magnetic field measurements, which is provided in the Level-2 FAC product of the Swarm project: see Ritter et al. (2013). The radial currents at off-equatorial regions are conventionally related to signatures of FACs (e.g., Lühr et al., 2019). Around the RED in Figure 3d, no conspicuous fluctuations of current density can be found, especially when we compare them with the current fluctuations scattered in other parts of this orbit.

3.4. Diamagnetic Effects of RED: Swarm Observation 2

Further details on the magnetic field variations (or equivalently, the current density variations) around the RED are shown in Figure 4. Only Swarm-Alpha data are presented here because the onboard absolute magnetometer onboard Swarm-Charlie failed in November 2014. In Figure 4a, we plot the plasma density measured by Swarm-Alpha as a function of MLAT. The RED is highlighted with red shading. The following three panels present the meridional, zonal, and compressional magnetic field residuals, respectively. The residuals are calculated by subtracting the CHAOS model values from the Swarm data, which can isolate magnetic field perturbations coming from the ionosphere. Both the Swarm Level-1b magnetic field data and CHAOS outputs are given in the local spherical coordinates: in the geographic north-south, east-west, and zenith-nadir directions. We make transformations from the original coordinate system to the mean-field-aligned frame. The new frame is defined by the CHAOS model magnetic field: the z-axis (parallel; compressional) aligned with the model magnetic field, y-axis (zonal) perpendicular to it on the horizontal plane, and x-axis completing the triad and pointing toward higher L-shells (meridional). The meridional and zonal components are shown in Figures 4b and 4c. The compressional component shown in Figure 4d is estimated by subtracting CHAOS outputs directly from the Absolute Scalar Magnetometer of Swarm-Alpha, which accurately measures absolute intensity of geomagnetic field.

In Figures 4b and 4c, we cannot identify conspicuous magnetic field deflections belonging to the RED. Large-scale ambient currents perpendicular to the geomagnetic field lines, when they encounter plasma irregularities such as EPBs, can diverge into the field-aligned direction, which creates FACs and resultant perturbations of zonal and meridional magnetic fields (e.g., Stolle et al., 2006; Yokoyama & Stolle, 2017). This phenomenon is analogous to electric currents in a simple circuit, which always find the easiest way to flow (i.e., the way with the minimum resistance). The absence of conspicuous FAC signatures in Figures 4b and 4c suggests that the RED cannot efficiently divert background perpendicular currents, possibly because the walls are not steep. The RED in this event has a smooth density profile while typical EPBs have precipitous walls with fine substructures (e.g., Figure 3a). The large conductivity gradients at EPB boundaries, unlike those of the RED, may efficiently divert background currents and generate observable FACs as reported in Rodríguez-Zuluaga and Stolle (2019), Stolle et al. (2006), and Yokoyama and Stolle (2017) .

Figure 4d presents the compressional component of the magnetic residuals. At the RED location, we can identify a clear shoulder structure sitting on a larger-scale declination trend. To aid visual inspection, we add a straight black dashed line drawn by hand. As the black dashed line is connected more or less smoothly to the compressional components outside the RED region, we argue that the shoulder structure protruding above the dashed line indicates RED. Ionospheric plasma density irregularities are known to seek a total pressure balance, which is the sum of magnetic and particle pressure. As a result, the magnetic field strength often increases within plasma depletions, which is the diamagnetic effect (e.g., Lühr et al., 2003; Rodríguez-Zuluaga et al., 2019; Stolle et al., 2006). We expect similar mechanisms at work for RED.

In Figure 4e, the magenta solid line represents the compressional magnetic residual in Figure 4d, but after passing a high-pass filter (based on a 251-point Savitzky-Golay filter) to remove the large-scale trend and to

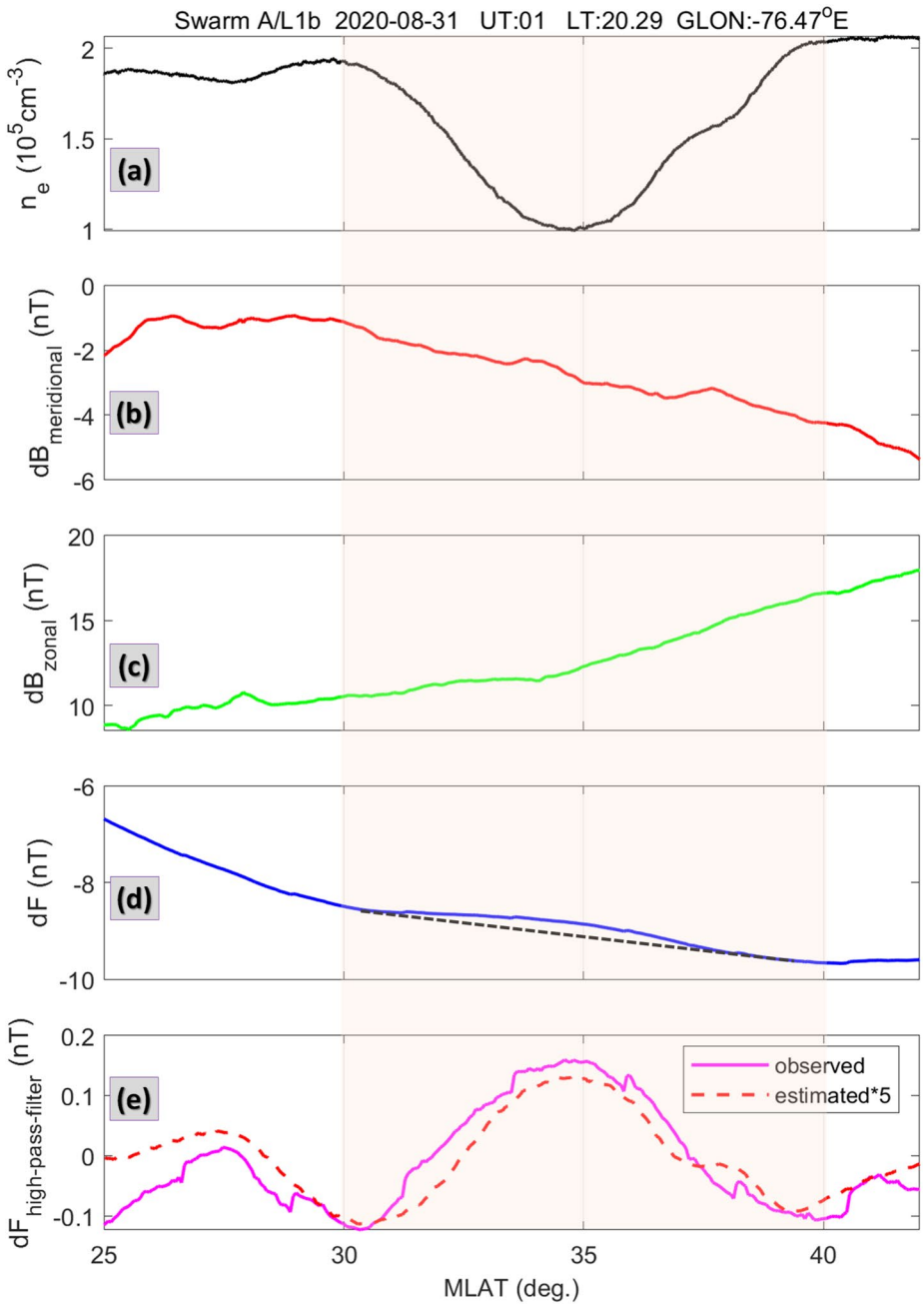

Figure 4. In-situ observations of the rocket exhaust depletion (RED) by Swarm-Alpha: (a) Plasma density, (b) meridional magnetic deflection toward higher L-shells, (c) zonal magnetic deflection toward magnetic east, (d) residual magnetic field strength, and (e) high-pass-filtered residual field strength (magenta solid line) and diamagnetic effect estimated from the plasma and magnetic data (red dashed line; intentionally magnified by a factor of 5). The RED event is highlighted with red shade.

isolate the RED signature. The red dashed curve corresponds to the diamagnetic effect calculated by inputting the measured plasma density (filtered in the same way as the compressional magnetic residual) and electron/ion temperature and background magnetic field intensity into Equation 3 of Rodríguez-Zuluaga et al. (2019), but intentionally magnified by a factor of 5. Note that the electron density and temperatures used for Figure 4 are recalibrated according to the recommendation in Lomidze et al. (2018). The "high-gain mode" equations in that paper are selected because the "Flags_LP" parameter during the RED event is unity (Probe 1 = high gain) except for a few data points during the sweep mode. "Flags_Te" parameter during the RED was always

20, which means that electron temperature data are reliable. In Figure 4e, the observed magnetic residual (after high-pass filtering; magenta solid line) peaks around the RED density minimum. Its MLAT profile closely follows the theoretically expected diamagnetic effect of the RED (red dashed line). But, the observed intensity (~0.3 nT peak-to-peak) is much larger than calculated from the plasma density depletion, approximately by a factor of five. We repeated the calculation with an assumption that ion temperature is equal to that of electrons: that is, with more emphasis on the electron temperature that was extensively validated by Lomidze et al. (2018) rather than on the recently released ion temperature data. But, the results were qualitatively similar to Figure 4 (figure not shown).

Previously (Park et al., 2008, 2010), reported that observed diamagnetic effects of natural ionospheric irregularities (e.g., EPBs) were stronger than expected from plasma density variations. Possible reasons may be effects of neutral pressure. For example, if the RED hosts more tenuous neutrals than the surrounding, the resultant particle pressure decrease can further enhance the magnetic field strength. Unfortunately, for neutral pressure, cross-validated high-resolution data are unavailable at the moment. The conjecture given above remains speculative. Note that the diamagnetic effect equation used for this study (Rodríguez-Zuluaga et al., 2019, Equation 3) assumes total pressure balance across ionospheric inhomogeneities. Hence, the difference between the expected diamagnetic effect and the actual magnetic field changes may imply possible pressure imbalance between the RED and the ambient. Further studies including neutral atmosphere observations are warranted to verify this conjecture.

Also, we note that the observed diamagnetic effect of about 0.3 nT is no larger than commonly observed dayside fluctuations of compressional magnetic field (e.g., Heilig et al., 2007, Figure 1; see also Heilig & Sutcliffe, 2016, Figure 2a). Therefore, for dayside RED it would be difficult to isolate the diamagnetic effect, if any, from natural background pulsations, which may explain why Park et al. (2015) reported no conspicuous diamagnetic effect.

4. Discussions

4.1. Vertical Structures of the RED

Vertical profiles of ionospheric density around the RED can be gleaned from the 3D COSMIC-2/GIS product. The GIS electron density data are produced by assimilating integrated plasma contents along the lines of sight, be they vertically upward (ground-based GPS receivers) or near-horizontal (COSMIC-2 occultation antennas), which inherently smooth out spatial inhomogeneity. Hence, rather than using the GIS plasma density as fiducial points for this RED event, we focus on qualitative changes of ionospheric vertical structures around the RED.

Figure 5 presents a selected set of the COSMIC-2/GIS data. The top and bottom rows correspond to 00 UT and 01 UT on 31 August 2020, respectively, which are approximately 0.5 and 1.5 hr after the launch. Note that the GIS product tagged with "00 UT" actually represents the time period between 00 UT and 01 UT. The left column shows electron density maps at a fixed altitudes of 280 km. The white solid and dashed contours indicate the dip equator and constant-MLAT lines, respectively. The thick black dashed line correspond to the reference line in Figure 2a. The right column presents vertical profiles of ionospheric density for two selected locations along the reference line on the map: red circle for the RED region, and the black triangle for the ambient plasma outside the RED. The blue horizontal dashed lines in Figures 5b and 5d represent the reference altitude (280 km) of the electron density maps in Figures 5a and 5c. We can see in Figures 5b and 5d that the chosen altitude of 280 km is close to the ionospheric peak height.

Two points in Figure 5 are worth discussion. First, plasma depletion around the launch site is reproduced by the COSMIC-2/GIS product at both 00 UT and 01 UT. The plasma depletion at 00 UT (Figure 5a) is not clearly isolated, but rather connected to adjacent depletions toward west. Considering that the TEC maps in Figure 1 show well-defined RED signatures, the slightly ambiguous signs of RED in Figure 5a seem to reflect inherent limitations the assimilation approach might have in reproducing localized plasma inhomogeneity. Also, according to Lin et al.(2020, Figure 7), the COSMIC-2/GIS product at the F-region peak has uncertainty of the order of 10^5 cm^{-3}, and the RED depth shown in Figure 5 is near this uncertainty level. The RED signature at 01 UT (bottom row) can be better identified in the global map (Figure 5c) around Cape Canaveral. The UT dependence of the RED behavior in the GIS product qualitatively agrees with Figure 1, where the RED was better developed around 01 UT (=25 UT) than near 00 UT (=24 UT).

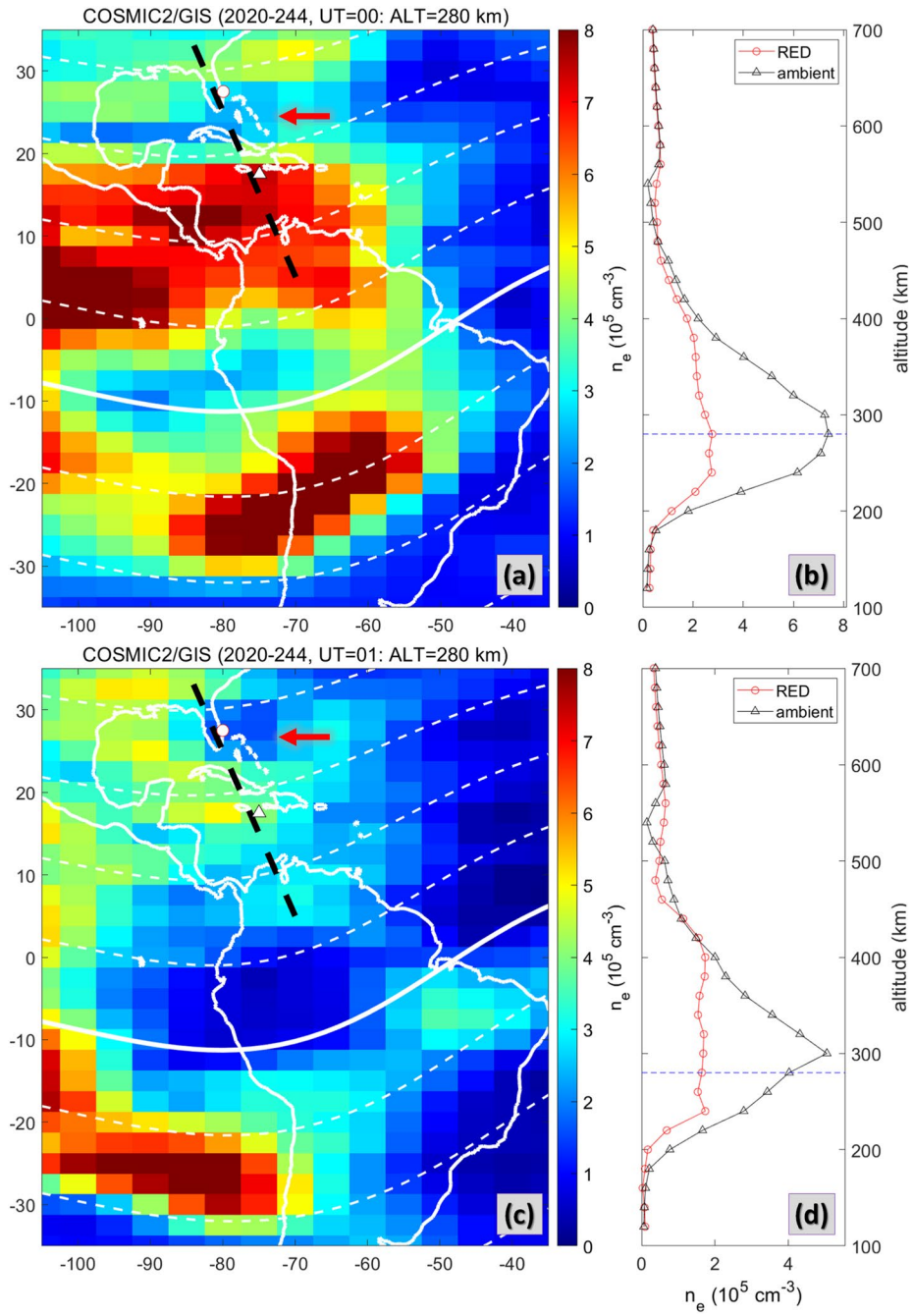

Figure 5. COSMIC-2/global ionospheric specification (GIS) data product around the rocket exhaust depletion (RED). The top and bottom rows correspond to 00 Universal Time (UT) (∼0.5 hr after the launch) and 01 UT (∼1.5 hr after the launch) on 31 August 2020, respectively. The left column corresponds to the constellation observing system for meteorology, ionosphere, and climate 2 (COSMIC-2)/GIS density maps at a chosen altitude of 280 km. The white solid and dashed contours on the maps respectively represent the dip equator and constant-magnetic latitudes lines. The thick black dashed line is the reference line used for the slab thickness estimation in Figure 7 (see also Figure 2). The right column presents vertical profiles of ionospheric density sampled at two locations on the map: Red circle for RED and black triangle for the ambient plasma, both of which are close to the reference line. The blue horizontal dashed lines in the rightmost column represent the 280 km height used for the COSMIC-2/GIS density maps in the left column. The RED regions are annotated with horizontal red arrows.

Second, the F-region vertical profiles in Figures 5b and 5d become blunter around RED (red curve) than in the ambient (black curve) at both 00 UT and 01 UT. For 01 UT (Figures 5c and 5d), where we can identify clear RED signatures, the slab thickness estimated from the COSMIC-2/GIS profiles (see Huang et al., 2016, Equation 2) is

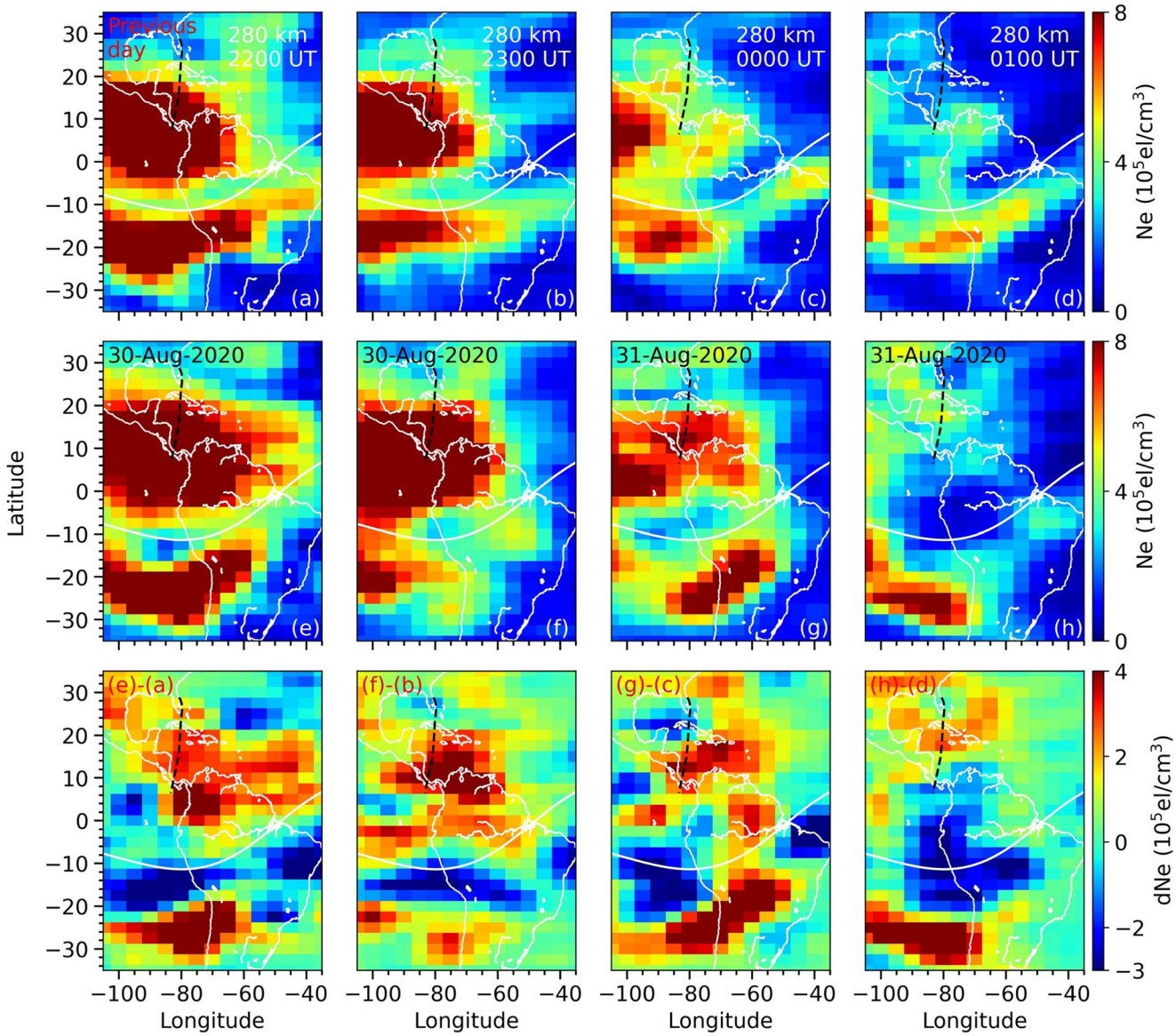

Figure 6. Extended time series of constellation observing system for meteorology, ionosphere, and climate 2/global ionospheric specification data product around the rocket exhaust depletion (RED) for the reference altitude of 280 km. The universal time flows from left to right columns. The top and middle rows correspond to the day before and the day of the rocket launch. An approximate trajectory of the launch is shown with a black dashed line in each panel. The bottom panel presents difference maps between the middle and top rows, which can isolated RED signatures from natural ionospheric variability.

288 and 168 km inside and outside RED, respectively. In other words, the slab thickness increased by approximately 70% near the RED. For 00 UT (Figure 5b), the increase was about 44%.

For completeness, in Figure 6 we show extended time series of COSMIC-2/GIS data at the 280 km altitude. The UT flows from left (22 UT) to right (01 UT on the next day). The top and middle rows present the GIS data on the previous day (29–30 August 2020) and the day of rocket launch (30–31 August 2020). Note that the rocket was launched around the time represented by Figure 6f, and the approximate trajectories (https://spaceflightnow.com/) are shown with a black dashed line in each panel. Figures 6g and 6h are reproduction of Figures 5a and 5c in a slightly different format. The bottom row is the difference between the middle and top rows, which would help to isolate the RED from natural ionospheric variabilities. In Figure 6, significant day-to-day variability in the spatial plasma distributions hinders us from clearly isolating the RED signal. Still, focusing on the region around the rocket launch (black dashed curves), we can at least find that: (a) RED signature emerges only after the launch of the rocket (bottom row), and (b) no RED-like signatures exist on the previous day (top row). Both

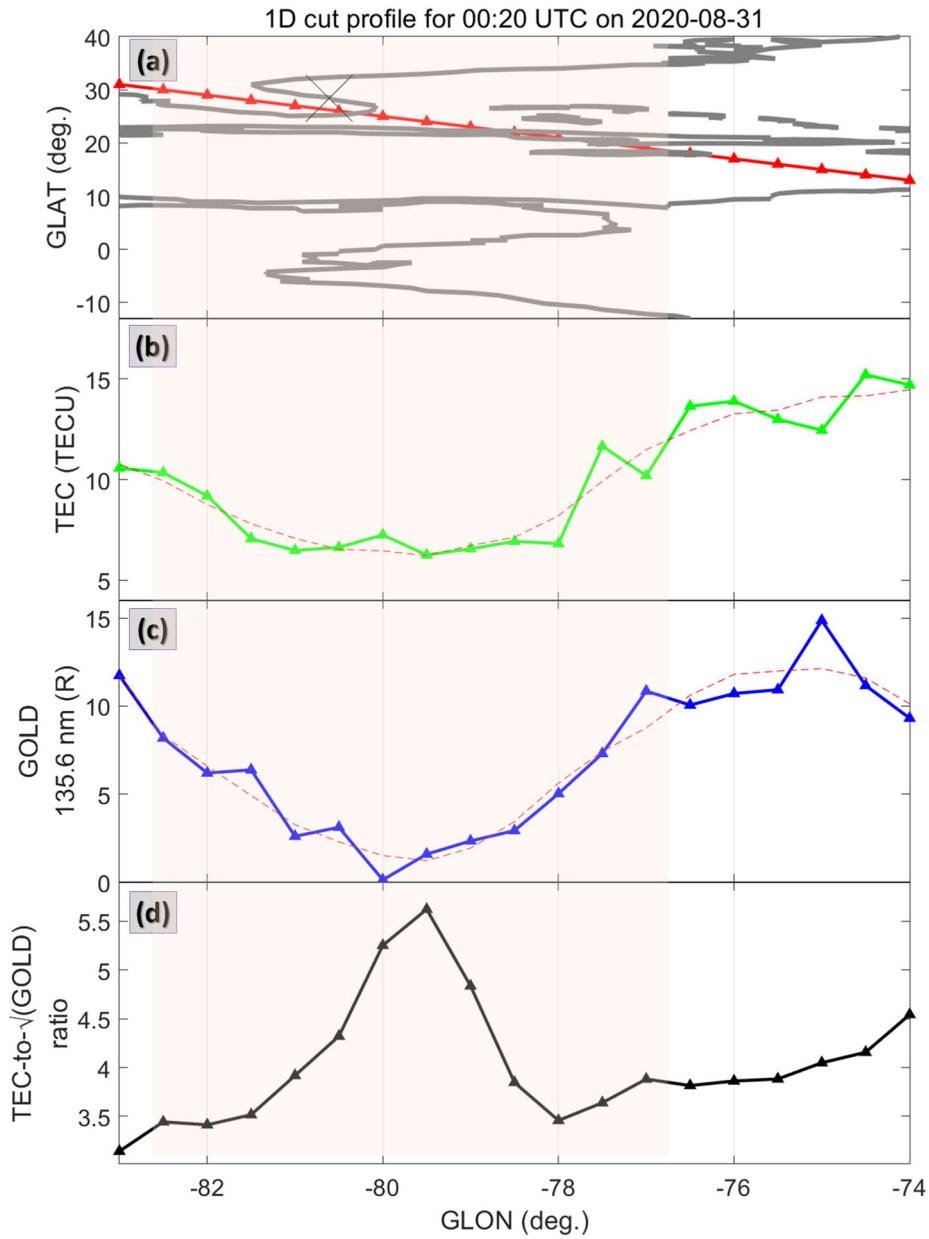

Figure 7. (a) Location of a one-dimensional reference line that passes through the rocket exhaust depletion event, (b) total electron content (TEC) along the reference line, (c) 135.6 nm nightglow in Figure 2 resampled along the reference line, and (d) the ratio between the smoothed TEC and the square root of the smoothed 135.6 nm nightglow. In panels b–c, the red dashed curves represent the data after passing a low-pass filter for smoothing.

features support that the COSMIC/GIS product qualitatively captured the RED event, which gives credence to the analyses given in this subsection.

In principle, the slab thickness can also be estimated from TEC and GOLD image. The TEC (Figure 1) and 135.6 nm nightglow image (Figure 2) are both related to vertically integrated contents of ionospheric plasma. While the former is simple line integral of electron density, the latter corresponds to that of the "squared" electron density. Note that square root of the 135.6 nm intensity is frequently used for a proxy of the F-region peak density (e.g., Rajesh et al., 2011, Figure 8). An important point here is that the TEC and 135.6 nm nightglow are not mutually redundant, and we may gain more information by combining the two. In Figure 7a, the red trace over a geographic map indicates the white dashed reference line in Figure 2. The reference line is used

for a representative 1-dimensional cut of the RED. Figures 7b and 7c present the TEC and 135.6 nm nightglow resampled along the reference line, respectively. The thin red dashed curves over-plotted in Figures 7b and 7c are the smoothed profiles with a second-order 9-point Savitzky-Golay filter. The RED region is highlighted with red shading. In Figure 7d, the ratio between TEC and the square root of 135.6 nm nightglow is presented. If we accept that the latter is proportional to the F-region peak density (e.g., Rajesh et al., 2011), the ratio in Figure 7d can be qualitatively deemed as the ionospheric slab thickness as defined by (Huang et al., 2016, Equation 2). The ratio is higher near the center of the RED than outside, which implies that the RED may have increased the slab thickness. In other words, the vertical profile of ionospheric density has a broad peak at the center of the RED and is sharper outside. In Figure 7d, the estimated slab thickness parameter increased from 3.5 to 5.5, that is, by about 57%. The relative increase roughly agrees with the results from COSMIC-2/GIS in Figures 5 and 6 (i.e., 44%–70%) and enhances the reliability of each other.

Note that we use only one GOLD map about 1 hr after the launch, a part of which is even contaminated by daylight. Therefore, the discussions on the slab thickness estimation from TEC and GOLD data should be further confirmed in the future with more RED events. Nevertheless, the approach described in this subsection demonstrates a new way of synergistically combining GOLD nighttime 135.6 nm measurements with TEC maps.

4.2. Density Spectra of the RED

In general, ionospheric density gradients are able to incur secondary smaller-scale irregularities: For example, see (Huba & Joyce, 2007, and references therein) and Sato et al. (2021). This subsection is dedicated to the question as to whether RED can also promote smaller-scale substructures. If it is actually the case, small-scale (smaller than the RED size) density fluctuations would be stronger within RED than in the neighborhood.

As Norsat-1 provides high-resolution plasma data (up to ∼1 kHz), we analyze their spectra in this subsection. Figure 8a presents Norsat-1/mNLP probe current (blue curve), which was shown as a proxy for plasma density in Figure 1, with the spacecraft GLAT (orange solid line) and GLON (orange dashed line) at its original altitude. The RED region is highlighted with a red rectangle. We apply the Welch's method (e.g., Ivarsen et al., 2019) to the probe current with a 1 min moving window stepping forward by 5 s. The resultant spectrogram is shown in Figure 8b. The 1 min window size corresponds to ∼500 km along the Norsat-1 track, which is smaller than the RED size. Hence, the spectrogram in Figure 8b generally represents scale sizes smaller than the RED, that is, substructures of RED. Note that the constant-frequency lines at multiples of ∼1 Hz are artifacts coming from the instrument and spacecraft bus.

Figure 8b shows that the power spectral density (PSD) is generally lower within the RED than outside. The PSD decrease from ∼02:49:30 UT appears to start prior to RED in Figure 8a. However, this apparent contradiction is due to the 1 min window size used for PSD estimation: for example, even if RED in Figure 8a started at 02:50 UT, it can affect PSD for the 1 min window at, for example, 02:49:10–02:50:10 UT. The PSD within RED is lower at earlier times (around 02:50 UT; poleward edge) than later (around 02:54 UT; equatorward edge). The conspicuous PSD depletion near 02:50 UT (Figure 8b) is not coincident with the minimum plasma density (near 02:52 UT in Figure 8a). The latitudinal offset between the PSD depletion and the plasma density minimum can be interpreted as the distribution of natural ionospheric irregularities, which are superposed on the RED-induced PSD trends. According to the ionospheric climatology in (Aol et al., 2020, Figure 6), nightside irregularities in this region (around Florida) and season (near September equinox) generally become stronger with decreasing latitudes. Similar latitude dependence can actually be seen throughout Figure 8b: For example, compare the PSD at 02:48 UT with that at 02:56 UT. We speculate that the latitude dependence of natural irregularities is superposed on the RED-induced PSD weakening, which leads to the latitudinal offset of the PSD minimum from the RED center. To say the least of it, we can argue that PSD inside the RED is overall lower than in the neighborhood. The low PSD could imply that the RED did not promote secondary instabilities for substructuring. It is also possible that density gradients caused by the RED did initiate secondary instabilities, but in the absence of an ongoing irregularity source mechanism, the free energy was quickly dissipated into the surrounding plasma. Since NorSat-1 passed the RED 3.5 hr after the relevant rocket launch, we cannot distinguish between the two interpretations.

Spectral slopes, that is, the steepness of each spectrum in the log-log space (e.g., Ivarsen et al., 2019), are given in Figure 8c. The 2 black horizontal lines in Figure 8b represent the scale size range used for slope evaluation (4–60 km). The range is conservatively chosen because PSD decreases significantly for scale sizes shorter than the

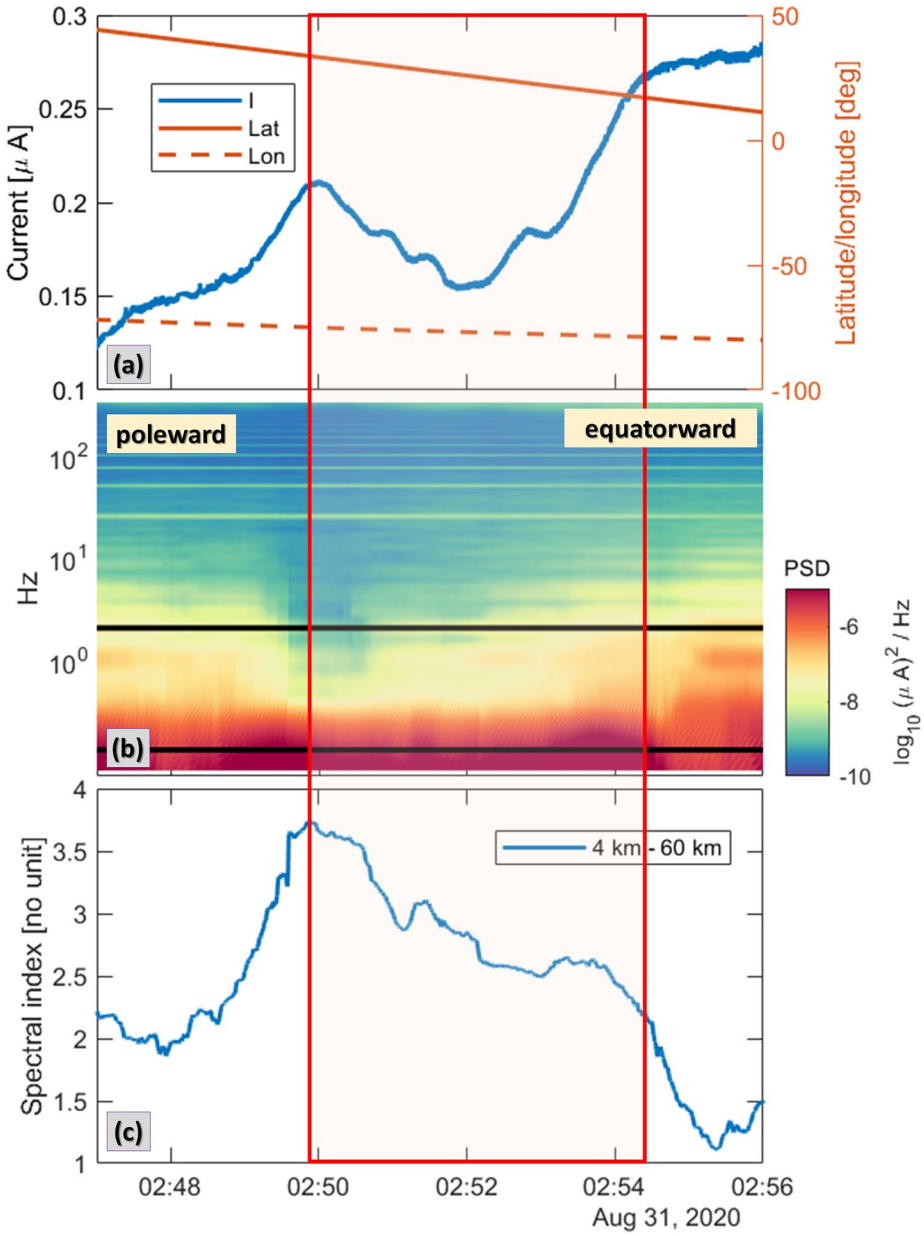

Figure 8. Spectral analyses of high-resolution Norsat-1/multi-needle Langmuir Probe data. The top panel presents probe currents (blue curve: Representing plasma density), geographic latitudes (orange solid line), and geographic longitudes (orange dashed line). The middle panel shows a spectrogram of the probe current with a 1 min moving window. In the bottom panel we give spectral indices (i.e., steepness of the spectra in the log-log space: See Ivarsen et al. (2019) for details) for the scale size range of 4–60 km. The rocket exhaust depletion is highlighted with a red rectangle.

4 km and is likely to be affected by noise. The spectral indices in Figure 8c increase inside the RED, which means softer spectra. In other words, irregularity weakening within the RED decreases with scale size; smaller-scale fluctuations are more severely damped. In summary, the RED accommodated weaker substructures (Figure 8b) and softer spectra (Figure 8c) than the ambient did. The results may be attributed to the following two facts: (a) As mentioned earlier, the RED does not seem to support enduring secondary instabilities that might inject new fluctuation energy, and (b) without energy injection, natural dissipation of ionospheric irregularities is faster for smaller scales (e.g., Ivarsen, St. Maurice et al., 2021, Equation 1).

However, note that NorSat-1 passed the RED 3.5 hr after the rocket launch, during which plasma inside and outside the RED region can be affected by other natural variabilities. All the quantitative discussions given above

should be confirmed by future studies with more RED events. Still, we can at least argue that the RED did not host substructures that are stronger and longer-lasting than those in the ambient plasma.

5. Summary and Conclusion

On 30–31 August 2020, a rocket was launched from Cape Canaveral, Florida and created plasma depletion as expected. The event lasted for more than 3 hr so as to be observed by multiple instruments. The combined observations revealed the following characteristics of the nighttime RED, which have been previously unexplored.

1. (FUV nightglow) The RED was observed by GOLD as 135.6 nm nightglow depletion.
2. (FAC and electron/ion temperature) The RED induced little changes of FAC or electron/ion temperature.
3. (diamagnetic effect) The RED enhanced magnetic field strength by about 0.3 nT. The magnetic deflections qualitatively agree with the diamagnetic effect, but are stronger in magnitude than simple calculations with only plasma density change. The quantitative discrepancy suggests a possible decrease of neutral pressure inside RED or pressure imbalance between the RED and the ambient plasma.
4. (slab thickness) According to COSMIC-2/GIS assimilation product, ionospheric slab thickness increased at the center of the RED by about half. This result is supported by the ratio between TEC and square root of the 135.6 nm intensity, which is a proxy of the slab thickness.
5. (RED density spectra) PSD analyses reveal that the nighttime RED did not host substructures that are stronger and longer-lasting than those of the ambient plasma.
6. (TEC versus in-situ plasma density). In-situ plasma density measured by LEO satellites near the RED qualitatively agrees with the corresponding TEC changes at the field-aligned footprints.

The results demonstrate the usefulness of GOLD and COSMIC-2/GIS in monitoring RED (and other natural irregularities) in multiple dimensions. The data sets can complement more conventional measures like TEC maps, ground-based all-sky cameras, and in-situ plasma diagnoses by LEO satellites. As GOLD regularly monitors one of the world's busiest launch sites, Cape Canaveral, we can continuously accumulate new information on RED, especially when GOLD is coordinated with other contemporaneous probes, such as COSMIC-2 and Swarm constellations.

Also, GOLD dayglow images of rocket launches are worth investigating in the future. Previous studies using FUV dayside disk images, some of which were already mentioned in Section 1, reported that the Lyman-alpha (121.6 nm) is enhanced at rocket exhaust. However, daytime rocket signatures in the GOLD wavelength range (132–162 nm) are largely unknown to the community. As the dayside 135.6 nm emissions are not solely representative of ionospheric plasma contents (e.g., Kil et al., 2013), RED signatures would not be directly seen. Still, because GOLD observes the same place multiple times, contributions of RED may be extracted from dayglow images by carefully devised methods for increasing signal-to-noise ratio.

Data Availability Statement

The data used for this study are available at the following web pages: (a) GOLD: https://gold.cs.ucf.edu/data/search/, (b) Madrigal TEC: http://cedar.openmadrigal.org/openmadrigal, (c) Swarm: https://swarm-diss.eo.esa.int/#swarm, (d) COSMIC-2/IVM: https://data.cosmic.ucar.edu/gnss-ro/cosmic2/postProc/level2/, (e) COSMIC-2/GIS: http://formosat7.earth.ncku.edu.tw/, and (f) Norsat-1: http://tid.uio.no/plasma/norsat/data.php.

Acknowledgments
The authors gratefully acknowledge fruitful discussions with Chao-Song Huang on the usage of TEC data and with Levan Lomidze and David Knudsen on the Swarm ion temperature products. The Swarm Ion Temperature Estimation (SITE) project has been supported as part of Swarm DISC activities, funded by ESA contact no. 4000109587. J. Park was supported by the National Research Council of Science & Technology (NST) grant by the Korea government (MSIT; No. CPS21161-120).

References

Aa, E., Zou, S., Ridley, A. J., Zhang, S.-R., Coster, A. J., Erickson, P. J., et al. (2019). Merging of storm time midlatitude traveling ionospheric disturbances and equatorial plasma bubbles. *Space Weather*, *17*, 285–298. https://doi.org/10.1029/2018SW002101

Aol, S., Buchert, S., & Jurua, E. (2020). Traits of sub-kilometre F-region irregularities as seen with the Swarm satellites. *Annals of Geophysics*, *38*, 243–261. https://doi.org/10.5194/angeo-38-243-2020

Bernhardt, P. A., Ballenthin, J. O., Baumgardner, J. L., Bhatt, A., Boyd, I. D., Burt, J. M., et al. (2012). Ground and space-based measurement of rocket engine burns in the ionosphere. *IEEE transactions on plasma science*, *40*(5), 1267– 1286.

Bernhardt, P. A., Huba, J. D., Kudeki, E., Woodman, R. F., Condori, L., & Villanueva, F. (2001). Lifetime of a depression in the plasma density over Jicamarca produced by space shuttle exhaust in the ionosphere. *Radio Science*, *36*(5), 1209–1220. https://doi.org/10.1029/2000RS002434

Bernhardt, P. A., & Sulzer, M. P. (2004). Incoherent scatter measurements of ring-ion beam distributions produced by space shuttle exhaust injections into the ionosphere. *Journal of Geophysical Research*, *109*, A02303. https://doi.org/10.1029/2002JA009693

Bhattarai, S. (2017). Interpretation of double Langmuir probe I-V characteristics at different ionospheric plasma temperatures. *American Journal of Engineering and Applied Sciences*, *10*, 882–889. https://doi.org/10.3844/ajeassp.2017.882.889

Booker, H. G. (1961). A local reduction of F-region ionization due to missile transit. *Journal of Geophysical Research*, *66*(4), 1073–1079. https://doi.org/10.1029/JZ066i004p01073

Chartier, A. T., Datta-Barua, S., McDonald, S., Bust, G. S., Tate, J., Goncharenko, L. P., et al. (2021). Night-time ionospheric localized enhancements (NILE) observed in North America following geomagnetic disturbances. *Journal of Geophysical Research: Space Physics*, *126*, e2021JA029324. https://doi.org/10.1029/2021JA029324

Chen, F. F. (2003). *Lecture notes on Langmuir probe diagnostics, mini-course on plasma diagnostics*. IEEE-ICOPS meeting. Retrieved from https://www.seas.ucla.edu/~ffchen/Publs/Chen210R.pdf

Cherniak, I., & Zakharenkova, I. (2018). Large-scale traveling ionospheric disturbances origin and propagation: Case study of the December 2015 geomagnetic storm. *Space Weather*, *16*, 1377–1395. https://doi.org/10.1029/2018SW001869

Choi, B.-K., & Kil, H. (2017). Large ionospheric TEC depletion induced by the 2016 North Korea rocket. *Advances in Space Research*, *59*(2), 532–541. https://doi.org/10.1016/j.asr.2016.09.012

Chou, M.-Y., Shen, M.-H., Lin, C. C. H., Yue, J., Chen, C.-H., Liu, J.-Y., & Lin, J.-T. (2018). Gigantic circular shock acoustic waves in the ionosphere triggered by the launch of FORMOSAT-5 satellite. *Space Weather*, *16*, 172–184. https://doi.org/10.1002/2017SW001738

Coster, A. J., Goncharenko, L., Zhang, S.-R., Erickson, P. J., Rideout, W., & Vierinen, J. (2017). GNSS observations of ionospheric variations during the 21 August 2017 solar eclipse. *Geophysical Research Letters*, *44*, 12041–12048. https://doi.org/10.1002/2017GL075774

Datta-Barua, S., Pedatella, N., Greer, K. R., Wang, N., Nutter, L., & Harvey, V. L. (2021). Lower thermospheric material transdsport via Lagrangian coherent structures. *Journal of Geophysical Research: Space Physics*, *126*, e2020JA028834. https://doi.org/10.1029/2020JA028834

Eastes, R. W., McClintock, W. E., Burns, A. G., Anderson, D. N., Andersson, L., Aryal, S., et al. (2020). Initial observations by the GOLD mission. *Journal of Geophysical Research: Space Physics*, *125*, e2020JA027823. https://doi.org/10.1029/2020JA027823

Feng, J., Guo, L., Xu, B., Wu, J., Xu, Z., Zhao, H., et al. (2021). Simulation of ionospheric depletions produced by rocket exhaust restricted by the trajectory. *Advances in Space Research*, 0273–1177. https://doi.org/10.1016/j.asr.2021.05.006

Heilig, B., Lühr, H., & Rother, M. (2007). Comprehensive study of ULF upstream waves observed in the topside ionosphere by CHAMP and on the ground. *Annals of Geophysics*, *25*, 737–754. https://doi.org/10.5194/angeo-25-737-2007

Heilig, B., & Sutcliffe, P. R. (2016). Coherence and phase structure of compressional ULF waves at low-Earth orbit observed by the Swarm satellites. *Geophysical Research Letters*, *43*, 945–951. https://doi.org/10.1002/2015GL067199

Hoang, H., Clausen, L. B. N., Røed, K., Bekkeng, T. A., Trondsen, E., Lybekk, B., et al. (2018). The multi-needle Langmuir probe system on board NorSat-1. *Space Science Reviews*, *214*, 75. https://doi.org/10.1007/s11214-018-0509-2

Huang, C.-S., de La Beaujardiere, O., Roddy, P. A., Hunton, D. E., Ballenthin, J. O., & Hairston, M. R. (2013). Long-lasting daytime equatorial plasma bubbles observed by the C/NOFS satellite. *Journal of Geophysical Research: Space Physics*, *118*, 2398–2408. https://doi.org/10.1002/jgra.50252

Huang, H., Liu, L., Chen, Y., Le, H., & Wan, W. (2016). A global picture of ionospheric slab thickness derived from GIM TEC and COSMIC radio occultation observations. *Journal Geophysical Research: Space Physics*, *121*, 867–880. https://doi.org/10.1002/2015JA021964

Huba, J. D., & Joyce, G. (2007). Equatorial spread F modeling: Multiple bifurcated structures, secondary instabilities, large density "bite-outs," and supersonic flows. *Geophysical Research Letters*, *34*, L07105. https://doi.org/10.1029/2006GL028519

Ivarsen, M. F., Jin, Y., Spicher, A., & Clausen, L. B. N. (2019). Direct evidence for the dissipation of small-scale ionospheric plasma structures by a conductive E region. *Journal of Geophysical Research: Space Physics*, *124*, 2935–2942. https://doi.org/10.1029/2019JA026500

Ivarsen, M. F., Park, J., Jin, Y., & Clausen, L. B. N. (2021). Ionospheric plasma fluctuations induced by the NWC very low frequency signal transmitter. *Journal of Geophysical Research: Space Physics*, *126*, e2021JA029213. https://doi.org/10.1029/2021JA029213

Ivarsen, M. F., St-Maurice, J.-P., Jin, Y., Park, J., Miloch, W., Spicher, A., et al. (2021). Steepening plasma density spectra in the ionosphere: The crucial role played by a strong E-region. *Journal of Geophysical Research: Space Physics*, *126*, e2021JA029401. https://doi.org/10.1029/2021JA029401

Kakinami, Y., Watanabe, S., Liu, J.-Y., & Balan, N. (2011). Correlation between electron density and temperature in the topside ionosphere. *Journal of Geophysical Research*, *116*, A12331. https://doi.org/10.1029/2011JA016905

Kakinami, Y., Yamamoto, M., Chen, C.-H., Watanabe, S., Lin, C., Liu, J.-Y., & Habu, H. (2013). Ionospheric disturbances induced by a missile launched from North Korea on 12 December 2012. *Journal Geophysical Research: Space Physics*, *118*, 5184–5189. https://doi.org/10.1002/jgra.50508

Kil, H., Lee, W. K., Shim, J., Paxton, L. J., & Zhang, Y. (2013). The effect of the 135.6 nm emission originated from the ionosphere on the TIMED/GUVIO/N2 ratio. *Journal of Geophysical Research: Space Physics*, *118*, 859–865. https://doi.org/10.1029/2012JA018112

Kil, H., Paxton, L. J., Jee, G., & Nikoukar, R. (2019). Plasma blobs associated with medium-scale traveling ionospheric disturbances. *Geophysical Research Letters*, *46*, 3575–3581. https://doi.org/10.1029/2019GL082026

Knudsen, D. J., Burchill, J. K., Buchert, S. C., Eriksson, A. I., Gill, R., Wahlund, J.-E., et al. (2017). Thermal ion imagers and Langmuir probes in the Swarm electric field instruments. *Journal of Geophysical Research: Space Physics*, *122*, 2655–2673. https://doi.org/10.1002/2016JA022571

Laundal, K. M., & Richmond, A. D. (2017). Magnetic coordinate systems. *Space Science Reviews*, *206*, 27. https://doi.org/10.1007/s11214-016-0275-y

Lin, C. H., Chen, C.-H., Matsumura, M., Lin, J.-T., & Kakinami, Y. (2017). Observation and simulation of the ionosphere disturbance waves triggered by rocket exhausts. *Journal of Geophysical Research: Space Physics*, *122*, 8868–8882. https://doi.org/10.1002/2017JA023951

Lin, C.-Y., Lin, C. C.-H., Liu, J.-Y., Rajesh, P. K., Matsuo, T., Chou, M.-Y., et al. (2020). The early results and validation of FORMOSAT-7/COSMIC-2 space weather products: Global ionospheric specification and ne-aided Abel electron density profile. *Journal of Geophysical Research: Space Physics*, *125*, e2020JA028028. https://doi.org/10.1029/2020JA028028

Liu, H., Ding, F., Yue, X., Zhao, B., Song, Q., Wan, W., et al. (2018). Depletion and traveling ionospheric disturbances generated by two launches of China's Long March 4B rocket. *Journal of Geophysical Research: Space Physics*, *123*, 10319–10330. https://doi.org/10.1029/2018JA026096

Lomidze, L., Burchill, J. K., Knudsen, D. J., & Huba, J. D. (2021). Estimation of ion temperature in the upper ionosphere along the swarm satellite orbits. *Earth and Space Science*, *8*, e2021EA001925. https://doi.org/10.1029/2021EA001925

Lomidze, L., Knudsen, D. J., Burchill, J., Kouznetsov, A., & Buchert, S. C. (2018). Calibration and validation of Swarm plasma densities and electron temperatures using ground-based radars and satellite radio occultation measurements. *Radio Science*, *53*, 15–36. https://doi.org/10.1002/2017RS006415

Lühr, H., Kervalishvili, G. N., Stolle, C., Rauberg, J., & Michaelis, I. (2019). Average characteristics of low-latitude interhemispheric and F region dynamo currents deduced from the swarm satellite constellation. *Journal of Geophysical Research: Space Physics*, *124*, 10631–10644. https://doi.org/10.1029/2019JA027419

Lühr, H., Rother, M., Maus, S., Mai, W., & Cooke, D. (2003). The diamagnetic effect of the equatorial Appleton anomaly: Its characteristics and impact on geomagnetic field modeling. *Geophysical Research Letters*, *30*, 1906. https://doi.org/10.1029/2003GL017407,17

Ma, X., Fang, H., Wang, S., & Chang, S. (2021). Impact of the ionosphere disturbed by rocket plume on OTHR radio wave propagation. *Radio Science*, *56*, e2020RS007183. https://doi.org/10.1029/2020RS007183

Meier, R. R., Plane, J. M. C., Stevens, M. H., Paxton, L. J., Christensen, A. B., & Crowley, G. (2010). Can molecular diffusion explain Space Shuttle plume spreading? *Geophysical Research Letters*, *37*, L08101. https://doi.org/10.1029/2010GL042868

Meier, R. R., Stevens, M. H., Plane, J. M. C., Emmert, J. T., Crowley, G., Azeem, I., et al. (2011). A study of space shuttle plumes in the lower thermosphere. *Journal of Geophysical Research*, *116*, A12322. https://doi.org/10.1029/2011JA016987

Mendillo, M., Rote, D., & Bernhardt, P. A. (1980). Preliminary report on the HEAO hole in the ionosphere. *Eos Transactions AGU*, *61*(28), 529. https://doi.org/10.1029/EO061i028p00529

Mendillo, M., Smith, S., Coster, A., Erickson, P., Baumgardner, J., & Martinis, C. (2008). *Man-made Space Weather* (6). Space Weather. https://doi.org/10.1029/2008SW000406

Nakashima, Y., & Heki, K. (2014). Ionospheric hole made by the 2012 North Korean rocket observed with a dense GNSS array in Japan. *Radio Science*, *49*, 497–505. https://doi.org/10.1002/2014RS005413

Niciejewski, R., Skinner, W., Cooper, M., Marshall, A., Meier, R. R., Stevens, M. H., et al. (2011). Verification of large-scale rapid transport in the lower thermosphere: Tracking the exhaust plume of STS-107 from launch to the Antarctic. *Journal of Geophysical Research*, *116*, A05302. https://doi.org/10.1029/2010JA016277

Oyama, K. I., Schlegel, K., & Watanabe, S. (1988). Temperature structure of plasma bubbles in the low latitude ionosphere around 600 km altitude. *Planetary and Space Science*, *36*(6), 553–567. https://doi.org/10.1016/0032-0633(88)90025-6

Park, J., Kil, H., Stolle, C., Lühr, H., Coley, W. R., Coster, A., & Kwak, Y.-S. (2016). Daytime midlatitude plasma depletions observed by Swarm: Topside signatures of the rocket exhaust. *Geophysical Research Letters*, *43*, 1802–1809. https://doi.org/10.1002/2016GL067810

Park, J., Lühr, H., & Min, K. W. (2010). Neutral density depletions associated with equatorial plasma bubbles as observed by the CHAMP satellite. *Journal of Atmospheric and Solar-Terrestrial Physics*, *72*, 157–163. https://doi.org/10.1016/j.jastp.2009.11.003

Park, J., Stolle, C., Lühr, H., Rother, M., Su, S.-Y., Min, K. W., & Lee, J.-J. (2008). Magnetic signatures and conjugate features of low-latitude plasma blobs as observed by the CHAMP satellite. *Journal of Geophysical Research*, *113*, A09313. https://doi.org/10.1029/2008JA013211

Park, J., Stolle, C., Xiong, C., Lühr, H., Pfaff, R. F., Buchert, S., & Martinis, C. R. (2015). A dayside plasma depletion observed at midlatitudes during quiet geomagnetic conditions. *Geophysical Research Letters*, *42*, 967–974. https://doi.org/10.1002/2014GL062655

Pignalberi, A., Giannattasio, F., Truhlik, V., Coco, I., Pezzopane, M., Consolini, G., et al. (2021). On the electron temperature in the topside ionosphere as seen by swarm satellites, incoherent scatter radars, and the international reference ionosphere model. *Remote Sensing*, *13*(20), 4077. https://doi.org/10.3390/rs13204077

Qin, J., Makela, J. J., Kamalabadi, F., & Meier, R. R. (2015). Radiative transfer modeling of the OI 135.6 nm emission in the nighttime ionosphere. *Journal of Geophysical Research: Space Physics*, *120*, 10116–10135. https://doi.org/10.1002/2015JA021687

Rajesh, P. K., Lin, C. H., Lin, C. Y., Chen, C. H., Liu, J. Y., Matsuo, T., et al. (2021). Extreme positive ionosphere storm triggered by a minor magnetic storm in deep solar minimum revealed by FORMOSAT-7/COSMIC-2 and GNSS observations. *Journal of Geophysical Research: Space Physics*, *126*, e2020JA028261. https://doi.org/10.1029/2020JA028261

Rajesh, P. K., Liu, J. Y., Hsu, M. L., Lin, C. H., Oyama, K. I., & Paxton, L. J. (2011). Ionospheric electron content and NmF2 from nighttime OI 135.6 nm intensity. *Journal of Geophysical Research*, *116*, A02313. https://doi.org/10.1029/2010JA015686

Ritter, P., Lühr, H., & Rauberg, J. (2013). Determining field-aligned currents with the Swarm constellation mission. *Earth Planets and Space*, *65*, 1285–1294. https://doi.org/10.5047/eps.2013.09.006

Rodríguez-Zuluaga, J., & Stolle, C. (2019). Interhemispheric field-aligned currents at the edges of equatorial plasma depletions. *Scientific Reports*, *9*, 1233. https://doi.org/10.1038/s41598-018-37955-z

Rodríguez-Zuluaga, J., Stolle, C., Yamazaki, Y., Lühr, H., Park, J., Scherliess, L., & Chau, J. L. (2019). On the balance between plasma and magnetic pressure across equatorial plasma depletions. *Journal of Geophysical Research: Space Physics*, *124*, 5936–5944. https://doi.org/10.1029/2019JA026700\

Sato, H., Kim, J. S., Otsuka, Y., Wrasse, C. M., Rodrigues de Paula, E., & Rodrigues de Souza, J. (2021). L-band synthetic aperture radar observation of ionospheric density irregularities at equatorial plasma depletion region. *Geophysical Research Letters*, *48*, e2021GL093541. https://doi.org/10.1029/2021GL093541

Ssessanga, N., Kim, Y. H., Choi, B., & Chung, J.-K. (2018). The 4D-var estimation of North Korean rocket exhaust emissions into the ionosphere. *Journal of Geophysical Research: Space Physics*, *123*, 2315–2326. https://doi.org/10.1002/2017JA024596

Stevens, M. H., Meier, R. R., Chu, X., DeLand, M. T., & Plane, J. M. C. (2005). Antarctic mesospheric clouds formed from space shuttle exhaust. *Geophysical Research Letters*, *32*, L13810. https://doi.org/10.1029/2005GL023054

Stolle, C., Lühr, H., Rother, M., & Balasis, G. (2006). Magnetic signatures of equatorial spread F as observed by the CHAMP satellite. *Journal of Geophysical Research*, *111*, A02304. https://doi.org/10.1029/2005JA011184

Vorburger, A., & Wurz, P. (2021). Modelling of possible plume mechanisms on Europa. *Journal of Geophysical Research: Space Physics*, *126*, e2021JA029690. https://doi.org/10.1029/2021JA029690

Wand, R. H., & Mendillo, M. (1984). Incoherent scatter observations of an artificially modified ionosphere. *Journal of Geophysical Research*, *89*(A1), 203–215. https://doi.org/10.1029/JA089iA01p00203

Yokoyama, T., & Stolle, C. (2017). Low and midlatitude ionospheric plasma density irregularities and their effects on geomagnetic field. *Space Science Reviews*, *206*, 495–519. https://doi.org/10.1007/s11214-016-0295-7

Zakharenkova, I., Astafyeva, E., & Cherniak, I. (2016). GPS and GLONASS observations of large-scale traveling ionospheric disturbances during the 2015 St. Patrick's Day storm. *Journal Geophysics Research Space: Physics*, *121*, 12138–12156. https://doi.org/10.1002/2016JA023332